Novel Materials

CHAPTER OUTLINE

18.1 GRAPHENE

18.1.1 Introduction

Carbon has four perfect crystalline forms: graphite, diamond, "Buckminsterfullerene" and a fullerene nanotube. In addition, graphene is a one-atom-thick allotrope of carbon, which is a honeycomb lattice of carbon atoms. Graphene also has two-dimensional Dirac-like excitations. We discussed the properties of graphene as well as its possible applications in electronics in Sections 10.7 and 10.8. In the following sections, we will discuss graphene as a building block for all novel materials of carbon as well as derive the theory of Dirac fermions discussed in Section 10.7.

One can view graphite as a stack of graphene layers, and carbon nanotubes can be considered as rolled cylinders of graphene. "Buckminsterfullerene" (C_{60}) can be viewed as molecules obtained by introducing pentagons on the hexagonal lattice of wrapped graphene. These are shown in Figure 18.1.

Diamond is not shown in the diagram because it is primarily used in making jewelry due to its beauty and elegance, and it does not have any major applications in materials science, presumably because of its cost. In addition, each atom in diamond is surrounded in all three directions in space by a full coordination. Because all directions are taken up, it would be nearly impossible for an atom in a diamond lattice to have any bonding with any other atom in the outside 3D space.

Graphene is a two-dimensional (2D) allotrope of carbon that can be imagined to be benzene rings stripped out from the hydrogen atoms. Fullerenes are molecules where carbon atoms are arranged spherically and are zero-dimensional (0D) objects that have discrete energy states. Fullerenes can be thought of as wrapped-up graphene because they are obtained from graphene with the introduction of pentagons, which create positive curvature defects. Carbon nanotubes, which have only hexagons and can be thought of as one-dimensional (1D) objects, are obtained by rolling graphene along a definite direction and reconnecting the carbon bonds. Graphite, which is a three-dimensional (3D) allotrope of carbon, is made out of stacks of graphene layers that are weakly coupled by van der Waals forces. Two-dimensional materials like graphene were presumed not to exist until 2004, when it was obtained in liquid suspension.[2] Graphene could also be obtained on top of noncrystalline substrates[3–5] and was eventually spotted in optical microscopes due to the subtle optical effects made by it on top of an SiO_2 substrate. Graphene exhibits high crystal quality, in which charge carriers can travel thousands of interatomic distances without scattering.

The Coulomb interactions are considerably enhanced in small geometries such as graphene quantum dots that lead to Coulomb blockade effects. The transport properties of graphene lead to a variety of applications, which range from single molecule detection to spin injection. Because
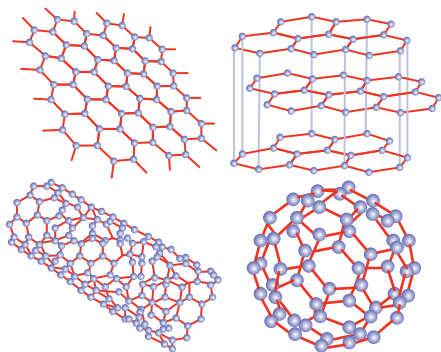

FIGURE 18.1

Clockwise: graphene (2D), graphite (3D), "Buckminsterfullerene" (0D), and carbon nanotubes (1D).

Reproduced from Castro Neto et al.[1] with the permission of the American Physical Society.

graphene has unusual structural and electronic flexibility, it can be tailored: deposition of metal atoms or molecules on top; incorporation of boron and/or nitrogen in its structure; and using different substrates that modify the electronic structure. The control of graphene properties can be extended in new directions that would allow for the creation of graphene-based systems with magnetic and superconducting properties.

18.1.2 Graphene Lattice

Carbon has four valence electrons, three of which form tight bonds with neighboring atoms in the plane. Their wave functions are of the form

$$\frac{1}{\sqrt{3}}\left(\psi_e(2s) + \sqrt{2}\psi_e(\tau_i 2p)\right), \quad (i = 1, 2, 3), \tag{18.1}$$

where $\psi_e(2s)$ is the $(2s)$ wave function for carbon, and $\psi_e(\tau_i 2p)$ are the $(2p)$ wave functions of which the axes are in the directions τ_i joining the graphite atom to its three neighbors in the plane. The fourth electron is in the $2p_z$ state. Its nodal plane is the lattice plane and its axis of symmetry perpendicular to it. Because the three electrons forming coplanar bonds do not play any part in the conductivity, graphene can be considered to have one conduction electron in the $2p_z$ state.

The unit cell of the hexagonal layer, designated as $PQRS$ in Figure 18.2, contains two carbon atoms A and B. The distance $AB \approx a = 1.42$ Å. The fundamental lattice displacements are $a_1 = AA'$ and $a_2 = AA''$, and their magnitude is $a_1 = \sqrt{3} \times 1.42$ Å $= 2.46$ Å. The reciprocal lattice vectors have magnitude $8\pi/3a$ and are in the directions AB and AS, respectively. Hence, the first Brillouin zone is a hexagon (see Figure 18.3) of which the sides are at a distance $4\pi/3a$ from its center. The density of electron states in **k** space is $2A$, where A is the area of the crystal. The zone has exactly one electron per atom. Therefore, the first Brillouin zone of graphene has $2N$ electron states, and the second Brillouin zone is empty. As we discussed in Sections 10.7 and 10.8, it becomes a semiconductor at finite temperatures.
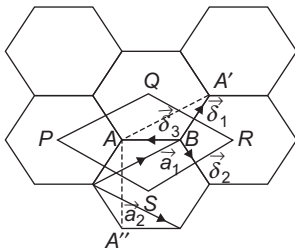

FIGURE 18.2

Honeycomb lattice structure of graphene, made out of two interpenetrating triangular lattices. The lattice unit vectors $\vec{a_1}$ and $\vec{a_2}$ and the nearest-neighbor vectors $\vec{\delta_1}, \vec{\delta_2}$, and $\vec{\delta_3}$. $AB = a$.
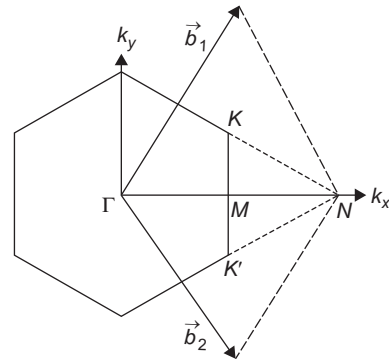

FIGURE 18.3

First Brillouin zone of the honeycomb lattice and the Dirac points K and K' at the corners.

The lattice vectors of graphene can be written as (Figure 18.2)

$$\mathbf{a}_1 = \frac{3a}{2}\left(\hat{x} + \frac{1}{\sqrt{3}}\hat{y}\right); \quad \mathbf{a}_2 = \frac{3a}{2}\left(\hat{x} - \frac{1}{\sqrt{3}}\hat{y}\right), \tag{18.2}$$

where the carbon–carbon distance is $a \approx 1.42$ Å. The reciprocal lattice vectors (shown in Figure 18.3) are given by (Problem 18.1)

$$\mathbf{b}_1 = \frac{2\pi}{3a}\left(\hat{x} + \sqrt{3}\hat{y}\right); \quad \mathbf{b}_2 = \frac{2\pi}{3a}\left(\hat{x} - \sqrt{3}\hat{y}\right). \tag{18.3}$$

The positions of the two Dirac points K and K', located at the corners of the Brillouin zone (of which the significance is to be explained later), are (Problem 18.2)

$$\mathbf{K} = \frac{2\pi}{3a}\left(\hat{x} + \frac{1}{\sqrt{3}}\hat{y}\right); \quad \mathbf{K}' = \frac{2\pi}{3a}\left(\hat{x} - \frac{1}{\sqrt{3}}\hat{y}\right). \tag{18.4}$$

The three nearest-neighbor vectors in real space are given by

$$\vec{\delta}_1 = \frac{a}{2}\left(\hat{x} + \sqrt{3}\hat{y}\right); \quad \vec{\delta}_2 = \frac{a}{2}\left(\hat{x} - \sqrt{3}\hat{y}\right); \quad \vec{\delta}_3 = -a\hat{x}. \tag{18.5}$$

The six second-nearest neighbors are located at $\vec{\delta}_1' = \pm\mathbf{a}_1$, $\vec{\delta}_2' = \pm\mathbf{a}_2$, and $\delta_3' = \pm(\mathbf{a}_2 - \mathbf{a}_1)$.

18.1.3 Tight-Binding Approximation

Wallace (Ref. 19) developed a "tight-binding" method for the band theory of graphite. Because the spacing of the lattice planes of graphite is large (3.37 Å) compared with the hexagonal spacing of the layer (1.42 Å), he neglected, as a first approximation, the interactions of the planes and assumed that conduction takes place in the layers. This is precisely graphene, which at that time was merely a concept. We note that some the notations have different values in that paper, presumably because it was published in 1947, but these have been modernized in the present derivation.

If $\chi(r)$ is the normalized orbital $2p_z$ wave function for an isolated atom, the wave function in the tight-binding approximation has the form

$$\psi = \phi_1 + \lambda\phi_2, \tag{18.6}$$

where

$$\phi_1 = \frac{1}{\sqrt{N}}\sum_A e^{i\mathbf{k}\cdot\mathbf{r}_A}\,\chi(\mathbf{r} - \mathbf{r}_A) \tag{18.7}$$

and

$$\phi_2 = \frac{1}{\sqrt{N}}\sum_B e^{i\mathbf{k}\cdot\mathbf{r}_B}\,\chi(\mathbf{r} - \mathbf{r}_B). \tag{18.8}$$

Here, the first sum is taken over A and all the lattice points generated from it by primitive lattice translations, and the second sum is similarly over the points generated from B (Figure 18.2). Neglecting the overlap integrals,

$$\int \chi(\mathbf{r} - \mathbf{r}_A)\chi(\mathbf{r} - \mathbf{r}_B)\,d\mathbf{r} = 0, \tag{18.9}$$

and substituting in Eq. (18.6),

$$H\psi = E\psi, \tag{18.10}$$

we obtain (Problem 18.3)

$$H_{11} + \lambda H_{12} = E \tag{18.11}$$

and

$$H_{12} + \lambda H_{22} = \lambda E. \tag{18.12}$$

Here,

$$H_{11} = H_{22} = \int \phi_1{}^* H\phi_2 d\nu; \quad H_{12} = H_{21}{}^* = \int \phi_1{}^* H\phi_2 d\nu \tag{18.13}$$

and

$$\int \phi_1{}^* \phi_1 d\nu = \int \phi_2{}^* \phi_2 d\nu = 1. \tag{18.14}$$

Eliminating λ from Eqs. (18.11) and (18.12), we obtain the secular equation

$$\begin{vmatrix} H_{11} - E & H_{12} \\ H_{21} & H_{22} - E \end{vmatrix} = 0. \tag{18.15}$$

From Eq. (18.15), it is easy to show that

$$E = \frac{1}{2}\left\{ H_{11} + H_{22} \pm \left((H_{11} - H_{22})^2 + 4|H_{12}|^2 \right)^{\frac{1}{2}} \right\}. \tag{18.16}$$

Because $H_{11} = H_{22}$, Eq. (18.16) can be rewritten in the alternate form

$$E_\pm = H_{11} \pm |H_{12}|. \tag{18.17}$$

The positive sign in Eq. (18.17) will apply to the outside of the hexagonal zone and the negative sign to the inside. The discontinuity of energy across the zone boundary is

$$\Delta E = 2|H_{12}|. \tag{18.18}$$

From Eqs. (18.7), (18.13), and (18.17), we obtain

$$H_{11} = \frac{1}{N} \sum_{A,A'} e^{-i\mathbf{k}\cdot(\mathbf{r}_A - \mathbf{r}_{A'})} \int \chi^* (\mathbf{r} - \mathbf{r}_A) H\chi(\mathbf{r} - \mathbf{r}_{A'}) \, d\nu. \tag{18.19}$$

Keeping only the nearest-neighbor integrals among the atoms A and writing

$$E_0 = \int \chi^* (\mathbf{r}) H\chi(\mathbf{r}) \, d\nu \tag{18.20}$$

and

$$\gamma_0' = -\int \chi^* (\mathbf{r} - \overrightarrow{\rho}') H\chi(\mathbf{r}) \, d\nu, \tag{18.21}$$

where $\overrightarrow{\rho}' = \mathbf{a}_1(say)$ is a vector joining the nearest neighbor among atoms A, we can show that (Problem 18.4)

$$H_{11} = E_0 - 2\gamma_0'\left[\cos\left(\sqrt{3}k_y a\right) + 2\cos\left(\frac{3}{2}k_x a\right)\cos\left(\frac{\sqrt{3}}{2}k_y a\right)\right]. \tag{18.22}$$

Writing

$$H = H_0 + (H - H_0), \tag{18.23}$$

where H_0 is the Hamiltonian of an isolated carbon atom, and using

$$H - H_0 = V - U < 0, \tag{18.24}$$

where U is the potential field of an isolated atom and V is the periodic potential of the lattice because

$$H_0\chi = \overline{E}\chi, \tag{18.25}$$

($\overline{E}$ is the energy of an electron in the $2p_z$ state in carbon), from Eqs. (18.20), (18.21), (18.24), and (18.25), we obtain

$$E_0 = \overline{E} - \int \chi^*(\mathbf{r})(U - V)\chi(\mathbf{r})\, d\nu \tag{18.26}$$

and

$$\gamma_0' = \int \chi^*(\mathbf{r} - \overrightarrow{\rho}')(U - V)\chi(\mathbf{r})\, d\nu > 0. \tag{18.27}$$

Similarly, we obtain the expression for H_{12},

$$H_{12} = \frac{1}{N}\sum_{A,B} e^{-i\mathbf{k}\cdot(\mathbf{r}_A - \mathbf{r}_B)}\int \chi^*(\mathbf{r} - \mathbf{r}_A)H\chi(\mathbf{r} - \mathbf{r}_B). \tag{18.28}$$

Considering only the nearest-neighbor interactions in the lattice (between atoms of type A and type B and vice versa), we write (in analogy with Eq. 18.27)

$$\gamma_0 = \int \chi^*(\mathbf{r} - \overrightarrow{\rho})(U - V)\chi(\mathbf{r})\, d\nu > 0, \tag{18.29}$$

where

$$\overrightarrow{\rho} = \mathbf{AB}. \tag{18.30}$$

It can be shown that (Problem 18.5)

$$H_{12} = -\gamma_0\left[e^{-ik_x a} + 2\cos\left(\frac{\sqrt{3}}{2}k_y a\right)e^{i\left(\frac{3}{2}k_x a\right)}\right] \tag{18.31}$$

and

$$|H_{12}|^2 = \gamma_0^2\left[1 + 4\cos^2\left(\frac{\sqrt{3}}{2}k_y a\right) + 4\cos\left(\frac{3}{2}k_x a\right)\cos\left(\frac{\sqrt{3}}{2}k_y a\right)\right]. \tag{18.32}$$

From Eqs. (18.22) and (18.32), we can write

$$E_{\pm}(\mathbf{k}) = H_{11} \pm H_{12} = E_0 - \gamma_0' f(\mathbf{k}) \pm \gamma_0 [3 + f(\mathbf{k})]^{1/2}, \tag{18.33a}$$

where

$$f(\mathbf{k}) = 2\left[\cos\left(\sqrt{3}k_y a\right) + 2\cos\left(\frac{3}{2}k_x a\right)\cos\left(\frac{\sqrt{3}}{2}k_y a\right) \right]. \tag{18.33b}$$

The energies at the various points in the Brillouin zone can be written as

$$\begin{aligned}
\Gamma&: E = E_0 - 3\gamma_0 - 6\gamma_0', \\
N&: E = E_0 + 3\gamma_0 - 6\gamma_0', \\
K&: E = E_0 + 3\gamma_0', \\
M\,(inside)&: E = E_0 - \gamma_0 + 2\gamma_0', \\
M\,(outside)&: E = E_0 + \gamma_0 + 2\gamma_0'.
\end{aligned} \tag{18.34a}$$

Across the boundary at any point over a side of the zone (Figure 18.3), there is a discontinuity of energy of amount

$$2\gamma_0\left[2\cos\left(\frac{\sqrt{3}}{2}k_y a\right) - 1 \right], \tag{18.34b}$$

which is a maximum at the center and decreases to zero at the corners. The degeneracy at K and similar points (called Dirac points) and the zero-energy gap at these points are consequences of the symmetry of the lattice and are independent of any approximation.

The energy contours are given by

$$E = E_0 - 3\gamma_0 - 6\gamma_0' + \frac{3}{4}(\gamma_0 + 6\gamma_0')(k_x^2 + k_y^2)\, a^2. \tag{18.35}$$

The curves of constant energy are shown in Figure 18.4.

It may be noted that near the corners K or K' (Dirac points),

$$|E - E_K| = 3\gamma_0' \pm \frac{3}{2}\gamma_0 |\mathbf{k} - \mathbf{K}| a - \frac{9}{4}\gamma_0' |\mathbf{k} - \mathbf{K}|^2 a^2. \tag{18.36}$$

The surfaces of constant energy are circular. If one neglects γ_0' relative to γ, Eq. (18.36) can be rewritten near the corners of the zone,

$$|E - E_K| \approx \frac{3}{2}\gamma_0 a |\mathbf{k} - \mathbf{K}| + O[(q/K^2)]$$

$$\approx \frac{3}{2}\gamma_0 a |\mathbf{q}| + O[(q/K^2)], \tag{18.37}$$

which can be rewritten in the alternate form

$$E_{\pm}(\mathbf{q}) \approx v_F |\mathbf{q}| + O[(q/K)^2], \tag{18.38}$$
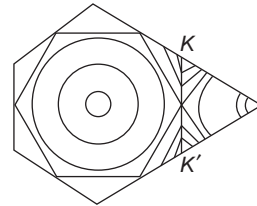

FIGURE 18.4

Curves of constant energy.

Reproduced from Wallace[19] with the permission of the American Physical Society.

where $\mathbf{q}$ is the momentum (in units $\hbar = 1$) measured relatively to the Dirac points, and v_F is the Fermi velocity,

$$v_F = 3\gamma_0 a/2. \tag{18.39}$$

The numerical value of $v_F \approx 1 \times 10^6$ m/s. From Eqs. (18.36) and (18.39), we obtain

$$E_{\pm}(\mathbf{q}) = 3\gamma_0' \pm v_F |\mathbf{q}| + O[(q/K)^2]. \tag{18.40}$$

Conduction in the graphene layer will take place through the electrons excited into the upper band and through the equal number of positive holes created in the lower band, as shown in Figure 18.5.

For moderate temperatures, $N(E)$ is even in $\in = |E - E_K|$ over the whole range in which the Fermi distribution $f(E)$ is different from its value at absolute zero. One can write $\xi = E_K$ and express

$$f(E) = f(\in) = 1/(e^{\in/k_B T} + 1). \tag{18.41}$$

It is interesting to note that the original tight-binding method, used by Wallace[19] in 1947 as a first approximation for the calculation of band structure of a single layer of graphite, is now being widely used to study the energy bands of graphene.

The tight-binding Hamiltonian for electrons in graphene can be written in the second-quantization form[1] (in units such that $\hbar = 1$),

$$\hat{H} = -t \sum_{<i,j>,\sigma} (\hat{a}_{i,\sigma}^\dagger \hat{b}_{j,\sigma} + H.c.) - t' \sum_{<<i,j>>,\sigma} (\hat{a}_{i,\sigma}^\dagger \hat{a}_{j,\sigma} + \hat{b}_{i,\sigma}^\dagger \hat{b}_{j,\sigma} + H.C.), \tag{18.42}$$

where $\hat{a}_{i,\sigma}^\dagger (\hat{a}_{i,\sigma})$ are the creation and annihilation operators with spin σ ($\sigma = \uparrow, \downarrow$) on site $\mathbf{R}_i$ on sublattice A, and $\hat{b}_{j,\sigma}^\dagger (b_{j,\sigma})$ are the corresponding operators on site $\mathbf{R}_j$ on sublattice B.

Here, $t(\approx 2.7$ eV$)$ is the nearest-neighbor hopping energy (between A and B), and $t' = -0.2\,t$ is the next nearest-neighbor hopping energy (between two A's or two B's). We note that $t = \gamma_0$ and $t' = \gamma_0'$ in Wallace's theory.

The electronic dispersion in the honeycomb lattice is shown in Figure 18.6, for finite values of $t = 2.7$ eV and $t' = -0.2\,t$. We also note the most striking difference between the results of Eq. (18.39) and the usual case in which $\in(\mathbf{q}) = \hbar^2 q^2/2m$, where m is the electron mass. In Eq. (18.39), the Fermi velocity v_F does not depend on the energy and momentum while in the usual case, $v = \hbar k/m = \sqrt{2E/m}$, and hence the velocity changes substantially with energy. We also note that the presence of the second-order terms (arising due to t' in Eq. 18.40) shifts in energy the position of the Dirac point and breaks the electron-hole symmetry.
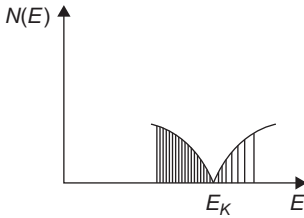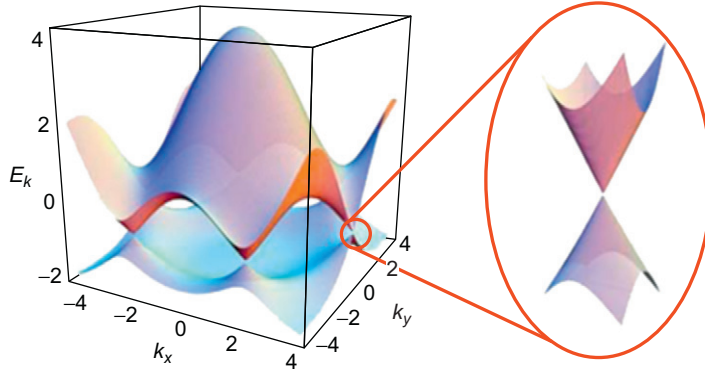

FIGURE 18.5

The form of the electronic energy states, $N(E)$, near E_K.

18.1.4 Dirac Fermions

Graphene's charge carriers have a particularly unique nature. Its charge carriers mimic relativistic particles and are described starting with the Dirac equation rather than the Schrodinger equation. The interaction of the electrons with the graphene's honeycomb lattice gives rise to new

FIGURE 18.6

Left: Energy spectrum (in units of t) for $t = 2.7$ eV and $t' = -0.2\,t$. Right: Close-up of the energy bands near to one of the Dirac points.

Reproduced from Castro Neto et al.[1] *with the permission of the American Physical Society.*

quasiparticles, which, at low energies E, are accurately described by the $(2 + 1)$-dimensional Dirac equation with an effective speed of light $v_F \approx 10^6 \, \text{m}^{-1}\text{s}^{-1}$. These quasiparticles are called massless Dirac fermions. They can be viewed as electrons that have lost their rest mass m_e or as neutrinos that have acquired the electron charge e. The reason the quasiparticles are known as Dirac fermions is as follows.

The Dirac equation for an electron in a periodic potential V can be written as

$$\hat{H}\phi_i = (c\,\overrightarrow{\alpha} \cdot \overrightarrow{p} + \beta m_e c^2 + IV)\phi_i = \varepsilon_i \phi_i, \tag{18.43}$$

where

$$\overrightarrow{\alpha} = \begin{bmatrix} 0 & \overrightarrow{\sigma} \\ \overrightarrow{\sigma} & 0 \end{bmatrix}, \quad \beta = \begin{bmatrix} E & 0 \\ 0 & -E \end{bmatrix}, \quad I = \begin{bmatrix} E & 0 \\ 0 & E \end{bmatrix}, \tag{18.44}$$

$\overrightarrow{\sigma}$ is the Pauli spin matrix vector, E is a 2×2 unit matrix, $\overrightarrow{p}$ is the momentum operator, m_e is the rest mass of the electron, and ϕ_i is a four-component Bloch function with an energy ε_i. The suffix i signifies a set of the wave vector, band index, and spin direction and is limited to positive energy states.

Graphene is a zero-gap semiconductor, in which low-E quasiparticles within each valley can be described by the Dirac-like Hamiltonian

$$\hat{H} = \hbar v_F \begin{pmatrix} 0 & k_x - ik_y \\ k_x + ik_y & 0 \end{pmatrix} = \hbar v_F \, \overrightarrow{\sigma} \cdot \overrightarrow{k}. \tag{18.45}$$

Eq. (18.43) can be approximated by Eq. (18.45) when the k-independent Fermi velocity v_F plays the role of the velocity of light c, $\overrightarrow{p} = \hbar \overrightarrow{k}$, and because the electrons are fermions, they are called Dirac fermions. The honeycomb lattice is made up of two equivalent carbon sublattices A and B, and the cosine-like energy bands associated with the sublattices intersect at zero E near the edges of the Brillouin zone, giving rise to conical sections of the energy spectrum. The electronic states at the intersection of the bands are composed of states belonging to the different sublattices, and their relative
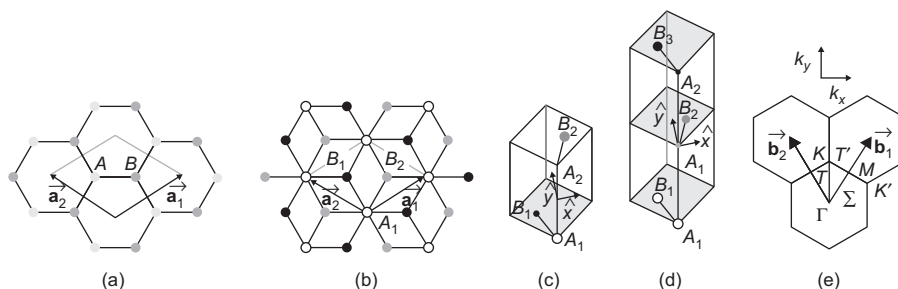
FIGURE 18.7

A top view of (a) unit cell of monolayer graphene, showing the inequivalent atoms A and B and unit vectors $\mathbf{a}_1$ and $\mathbf{a}_2$; (b) real-space bilayer graphene in which the light-/dark-gray dots and black circles/black dots represent the carbon atoms in the upper and lower layers; (c) the unit cell and the $\hat{x}$ and $\hat{y}$ unit vectors of bilayer graphene; (d) the same as (c) for trilayer graphene; and (e) the reciprocal space unit cell showing the first Brillouin zone with its high symmetry points.

Reproduced from Malard et al.[12] with the permission of Elsevier.

contributions are taken into account by using two-component wave functions (spinors). The index to indicate sublattices A and B is known as pseudospin $\overrightarrow{\sigma}$ because it is similar to the spin index (up and down) in quantum electrodynamics (QED). The real spin of the electrons must be described by additional terms in the Hamiltonian. Because the QED-specific phenomena are often inversely proportional to c and because $c/v_F \approx 300$, the pseudospin effects usually dominate over those due to the real spin.

One can introduce the concept of chirality, which is formally a projection of $\overrightarrow{\sigma}$ on the direction of motion $\overrightarrow{k}$, and is positive (negative) for electrons (holes). Chirality in graphene signifies the fact that $\overrightarrow{k}$ electrons and $-\overrightarrow{k}$ hole states originate from the same sublattice. The concepts of chirality and pseudospin are important because they are conserved quantities.

18.1.5 Comprehensive View of Graphene

A comprehensive view of the unit cell of monolayer, bilayer, and trilayer graphene and the first Brillouin zone with its high symmetry points are shown in Figure 18.7.

18.2 FULLERENES

18.2.1 Introduction

If one forms a vapor of carbon atoms and lets them condense slowly while keeping the temperature high, as the intermediate species grow, there is a path where the bulk of all reactive kinetics follows that make spheroidal fullerenes. There are two types of fullerenes that are famous for different reasons. The "Buckminsterfullerene" (C_{60}) is the most symmetric of all possible molecules. In addition, it is possible by adding a few percent of other atoms (nickel and cobalt) to trick the carbon into making tubes. The (10,10) fullerene nanotube is the most famous nanotube. The propensity for bonding that causes C_{60} to be the end point of 30–40% of all the reactive kinetics leads to the (10,10)

nanotube. The metal atoms (nickel and cobalt) prevent the addition of the seventh, eighth, and ninth pentagons, and ultimately, the growing tubelet can anneal to its most energetically favored form.

The idea that C_{60} would form a stable molecule originated from Euler's rule stating that a solid figure with any even number n of 24 or more vertices could be constructed with 12 pentagons and $(n-20)/2$ hexagons. The spheroidal carbon–cage carbon molecules consisting only of pentagons and hexagons were given the generic name "fullerenes."

18.2.2 Discovery of C_{60}

The truncated icosahedron form of C_{60} is shown in Figure 18.8. It was discovered by Kroto et al.[9] by using a supersonic laser-vaporization nozzle source, as shown in Figure 18.9a.

C_{60} is chemically a very stable structure. Cluster "cooking" reactions in the "integrating cup" were responsible for the C_{60} cluster's becoming over 50 times more intense than any other cluster in the nearby size range. The up-clustering reactions with small carbon chains and rings reacted away nearly all clusters except for C_{60}, which survived because of its perfect symmetry. C_{60} does not have any dangling bonds because the valences of every carbon atom are satisfied. There is no specific point of chemical attack because every atom is equivalent by symmetry. While curving the intrinsically planar system of double bonds into a spherical shape, strain is introduced. However, this strain is uniformly and symmetrically distributed over the molecule. No other structure has this high degree of symmetry, and hence, the experimental observation that carbon-vapor condensation conditions could be found where the intensity of the mass spectrum peak of the C_{60} in the carbon cluster beam was many times the intensity of any of its near neighbors in mass is shown in Figure 18.9b.
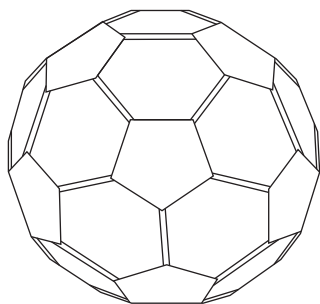

FIGURE 18.8

Truncated icosahedron C_{60}, popularly known as "Buckminsterfullerene."

Reproduced from Curl[2] with the permission of the American Physical Society.
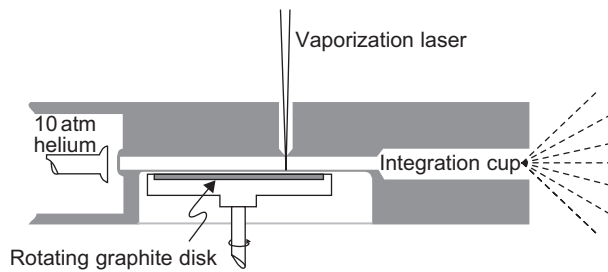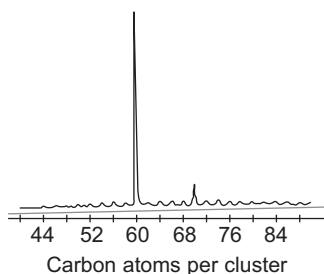

FIGURE 18.9a

Schematic cross-sectional drawing of the supersonic laser-vaporization nozzle source used in the discovery of fullerenes.
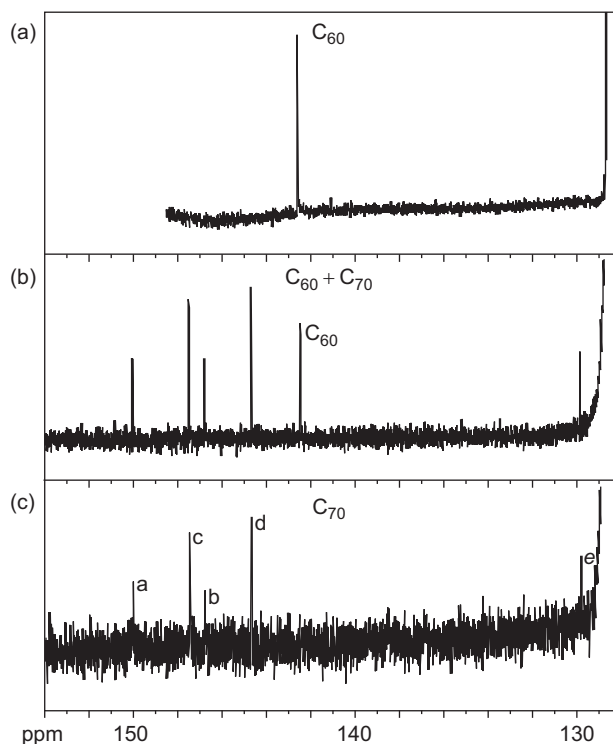
Reproduced from Smalley[16] with the permission of the American Physical Society.

FIGURE 18.9b

Intensity of the mass spectrum peak of the C_{60} in the carbon cluster beam relative to its neighbors in mass.

Reproduced from Curl[2] with the permission of the American Physical Society.

To confirm the existence of C_{60}, Kroto and coworkers[9] made two pioneering NMR experiments. The first experiment was done on a solution of C_{60} with benzene, which yielded a very strong resonance line at 128 ppm (for benzene) and a very tiny NMR trace in which C_{60} resonance was identified at 143 ppm. However, a second experiment (Ref. 18) in which C-NMR spectrum obtained from chromatographically purified samples of soluble material extracted from arc-processed graphite, yielded a spectrum of purified C_{60}, in which a strong resonance was obtained at 143 ppm. This result is shown in Figure 18.10.

FIGURE 18.10

C-NMR spectrum of (a) purified C_{60} (143 ppm); (b) mixed sample; (c) purified C_{70} (five lines).

Reproduced from Kroto[8] with the permission of the American Physical Society.

The fullerenes have a wide variety of technological applications. An example of a fullerene-based *n*-channel FET is shown in Figure 18.11. A highly doped *n*-type silicon wafer takes the place of the gate metal, a $\sim$30−300 nm thick layer of SiO_2 serves as the oxide, and the fullerene film serves as the semiconductor.

When an appropriate positive gate voltage V_G is applied, the drain current I_D increases, which indicates that a conduction channel is formed near the fullerene-insulator interface.

Another application of fullerene is in C_{60} photolithography. The sequence of steps (deposition, exposure, development, and pattern transfer) used in photolithography, in which C_{60} acts as a negative photoresist, is shown in Figure 18.12.

One of the many important potential applications of fullerenes is the nature of the fullerenes and metallic and semiconductor substrates. Direct rectification between solid C_{60} and *p*-type crystalline Si has been shown in $Nb/Co_{60}/p$-Si and $Ti/Co_{60}/p$-Si heterojunctions, which are strongly rectifying. Because the potential barriers at the Nb-C_{60} and Ti-C_{60} interfaces are close to
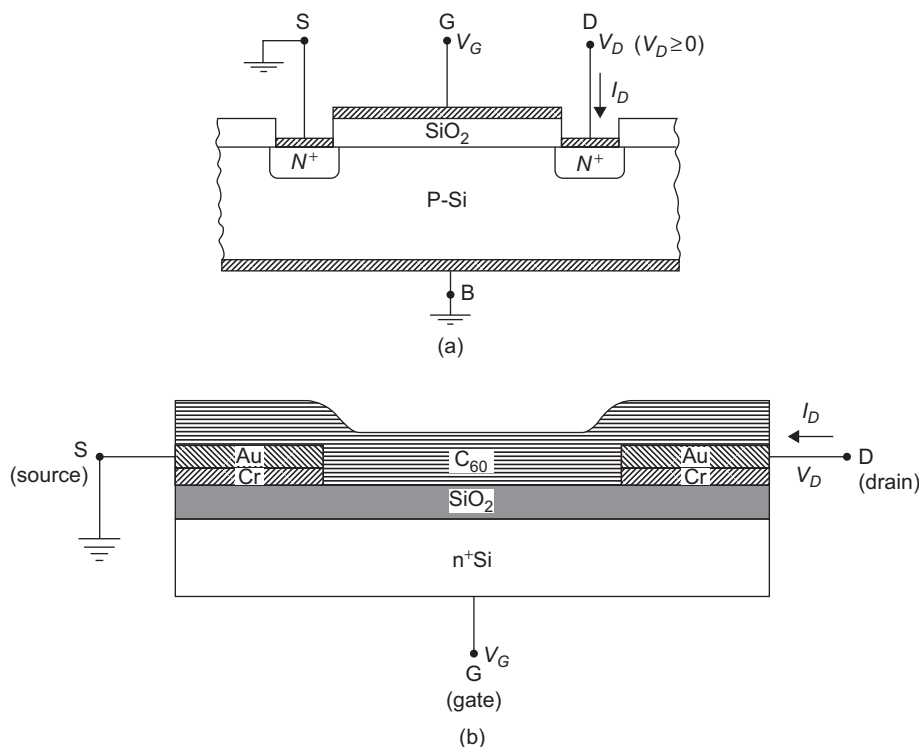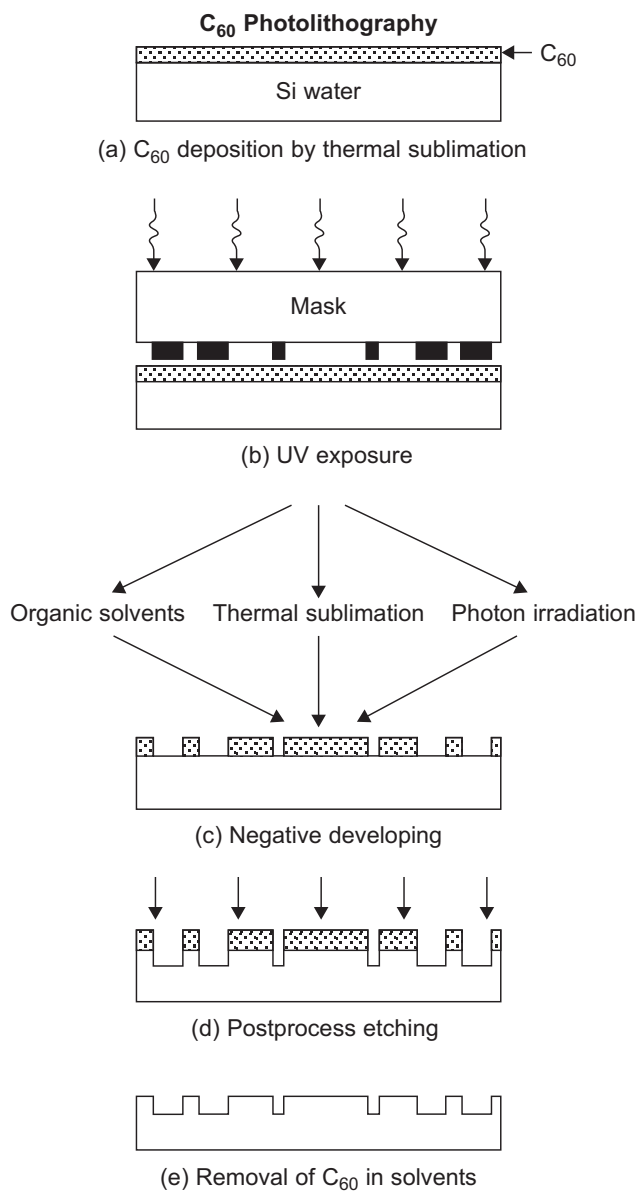

FIGURE 18.11

(a) The terminal designations and blasting conditions for Si-based MOSFETs. G, D, B, and S, respectively, denote the ground, drain, base, and source. (b) The corresponding structure for the fullerene C_{60} device.

Reproduced from Dresselhaus et al.[3] with the permission of Elsevier.

FIGURE 18.12

Sequence of steps of C_{60} photolithography.

Reproduced from Dresselhaus et al.[3] with the permission of Elsevier.
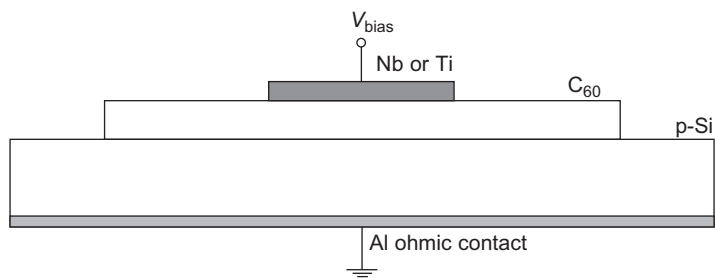
FIGURE 18.13

Schematic cross-section of an Nb/C_{60}/p-Si structure used as a heterojunction diode.

*Reproduced from Dresselhaus et al.[3] with the permission of Elsevier.*

zero, it is the C_{60}/p-Si interface that is responsible for the strong rectifying properties of the heterostructure. A schematic cross-section of the Nb/C_{60}/p-Si interface is shown in Figure 18.13.

18.3 FULLERENES AND TUBULES
18.3.1 Introduction

The fullerene nanotube (10,10) mentioned in the introduction of the previous section, with one end open, is shown in Fig. 18.14. The (10,10) tube is formed because the metal atoms frustrate the ability of the open edge to curve in and close. The addition of the seventh, eighth, and ninth pentagons is prevented, and by appropriate choice of temperature and reaction rate, the growing tubelet can anneal to its most energetically favored form.

The closed end is a hemifullerene dome (one half of C_{240}), whereas the other end is left open. These ends are directly amenable to the formation of excellent C-O, C-N, or C-C covalent bonds to attach any molecule, enzyme, membrane, or surface to the end of the tube. If two objects *A* and *B* are attached to the two ends, they will communicate with each other by metallic transport along the tube. Thus, the (10,10) tube is a metallic wave guide for electrons.
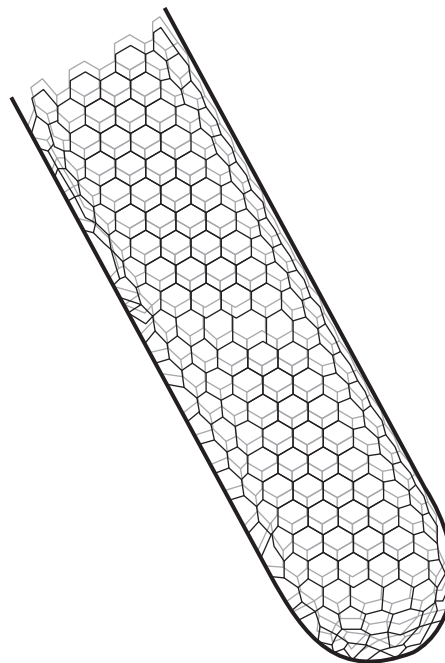
FIGURE 18.14

Section of a (10,10) fullerene nanotube with one end open.

18.3.2 Carbon Nanotubeles

It is convenient to specify a general carbon nanotubule in terms of the tubule diameter d_t and the chiral angle θ, which are shown in Figure 18.15 as the rectangle bounded by the chiral vector **OA** or $\mathbf{C}_h$. The chiral vector

$$\mathbf{C}_h = n\mathbf{a}_1 + m\mathbf{a}_2 \qquad (18.46)$$

is defined on the honeycomb lattice by unit vectors $\mathbf{a}_1$ and $\mathbf{a}_2$. $\mathbf{C}_h$ connects two crystallographically equivalent sites O and A on a two-dimensional graphene sheet where a carbon atom is located at each vertex of the honeycomb structure. Figure 18.15 shows the chiral angle θ of the nanotube with respect to the zigzag direction ($\theta = 0$) and the unit vectors $\mathbf{a}_1$ and $\mathbf{a}_2$ of the hexagonal honeycomb lattice. The armchair tubule (Figure 18.16a) corresponds to $\theta = 30°$ on this construction. An ensemble of chiral vectors can be specified by Eq. (18.46) in terms of pairs of integers (n, m), and this ensemble is shown in Figure 18.17. Each pair of integers (n, m) defines a different set of rolling the graphene sheet to form a carbon nanotube.

Along the zigzag axis $\theta = 0°$. Also shown in the figure is the basic translation vector $\mathbf{OB} = \mathbf{T}$ of the 1D tubule unit cell, and the rotation angle ψ and the translation τ, which constitute the basic symmetry operation $R = (\psi | \tau)$. The integers (n, m) uniquely determine the tubular diameter d_t and θ. The diagram is constructed for $(n, m) = (4, 2)$.
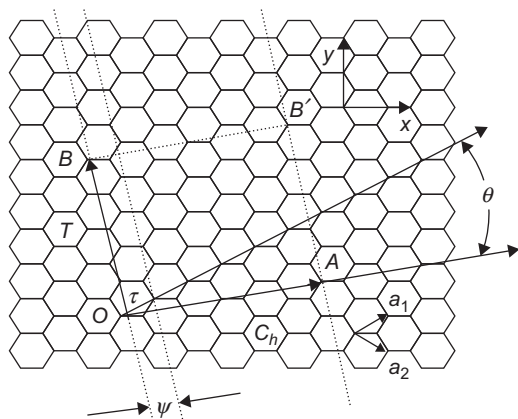
18.3.3 Three Types of Carbon Nanotubes

When the two ends of the vector $\mathbf{C}_h$ are superimposed, the cylinder connecting the two hemispherical caps of Figure 18.16 is formed. The line AB' (in Figure 18.15) is joined to the parallel line OB, where the lines OB and AB' are perpendicular to the vectors $\mathbf{C}_h$ at each end. There are no distortions of the bond angles in the chiral tubule except the distortions caused by the cylindrical curvature of the tubule. Differences in the tubular diameter d_t give rise to the differences in the various properties of carbon nanotubes. The vectors $(n, 0)$ denote zigzag tubules, and the vectors (n, n) denote armchair tubules. The larger the value of n, the larger the tubule diameter. The $(n, 0)$ and (n, n) have high symmetry and exhibit a mirror symmetry plane normal to the tubular axis. The other vectors (n, m) correspond to chiral nanotubes. Because both right- and left-handed chirality are

FIGURE 18.15

The 2D graphene sheet is shown along with the vector that specifies the chiral nanotube.
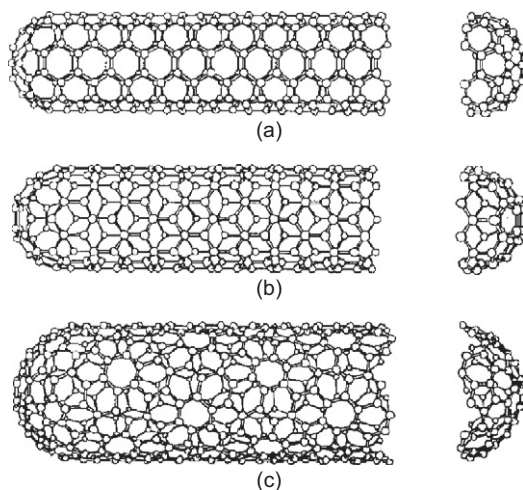
FIGURE 18.16

Three types of nanotubes obtained by rolling a graphene sheet into a cylinder and capping each end of the cylinder with half of a fullerene molecule; a "fullerene-derived tubule" that is one atomic layer in thickness is formed: (a) $\theta = 30°$ (an armchair tubule); (b) $\theta = 0°$ (a) zigzag tubule; and (c) chiral tubule.

Reproduced from Dresselhaus et al.[4] with the permission of Elsevier.

possible for chiral nanotubes, the chiral tubules are optically active to either right- or left-circularly polarized light propagating along the tubule axis.

The tubular diameter d_t is given by

$$d_t = C_h/\pi = \sqrt{3}a_{C-C}(m^2 + mn + n^2)^{1/2}/\pi, \tag{18.47}$$

where a_{C-C} is the nearest-neighbor C–C distance, C_h is the length of the chiral vector $\overrightarrow{C_h}$, and the chiral angle θ is given by

$$\theta = \tan^{-1}[\sqrt{3}m/(m + 2n)]. \tag{18.48}$$

The three types of carbon nanotubes are shown in Figure 18.16.

Figure 18.17 shows the number of distinct caps that can be formed theoretically from pentagons and hexagons, such that each cap fits continuously onto the cylinder of the tubule, specified by a given (n, m) pair. It shows that the hemispheres of C_{60} are the smallest caps that satisfy these requirements, so that the smallest carbon nanotube is expected to be $7\,\text{Å}$, which is in agreement with the experiment. Figure 18.17 also shows that the number of possible caps increases rapidly with increasing tubular diameter. Below each pair of integers (n, m) is listed the number of distinct caps that can be joined continuously to the cylindrical carbon tubule denoted by (n, m).

Due to the point group symmetry of the honeycomb lattice, several values of (n, m) will give rise to equivalent nanotubes. Therefore, one restricts consideration to the nanotubes arising from the $30°$ wedge of the 3D Bravais lattice shown in Figure 18.17. Because the length-to-diameter ratio of
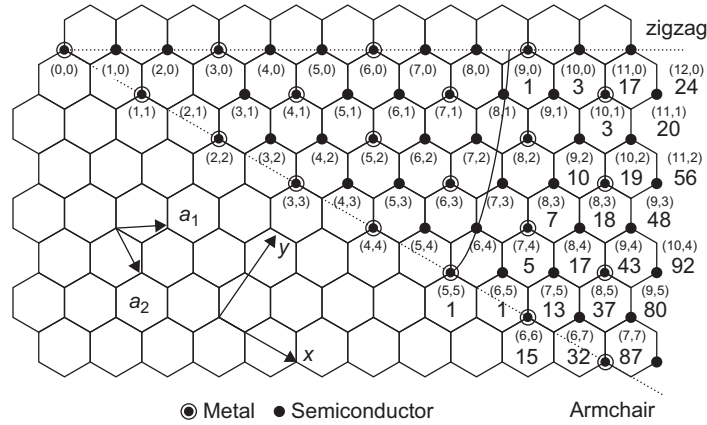
FIGURE 18.17

The 2D graphene sheet that specifies the chiral nanotube.

carbon nanotubes is $>10^3$ while the diameter is only ~ 10 Å, carbon nanotubes are an important system for studying one-dimensional physics.

18.3.4 Symmetry Properties of Carbon Nanotubes

To study the properties of carbon nanotubes as 1D systems, we define the lattice vector $\mathbf{T}$ along the tubule axis normal to the chiral vector $\mathbf{C}_h$ defined in Eq. (18.46) and Figure 18.15. The vector $\mathbf{T}$ defines the unit cell of the 1D carbon nanotube. The length T of the translation vector $\mathbf{T}$ corresponds to the first lattice point of the 2D graphene sheet through which the vector $\mathbf{T}$ passes. Thus, we obtain from Figure 18.15 and these definitions

$$\mathbf{T} = [(2m+n)\mathbf{a}_1 - (2n+m)\mathbf{a}_2]/d_R, \tag{18.49}$$

with a length

$$T = \sqrt{3}C_h/d_R. \tag{18.50}$$

The length C_h is defined in Eq. (18.47). Defining d as the highest common divisor of (n,m), we have

$$d_R = \begin{cases} d \text{ if } n-m \text{ is not a multiple of } 3d \\ 3d \text{ if } n-m \text{ is a multiple of } 3d. \end{cases} \tag{18.51}$$

The relation between the fundamental symmetry vector $\mathbf{R} = p\mathbf{a}_1 + q\mathbf{a}_2$ of the 1D unit cell and the two vectors that specify the carbon nanotube (n,m), the chiral vector $\mathbf{C}_h$, and translation vector $\mathbf{T}$ are shown in Figure 18.18.
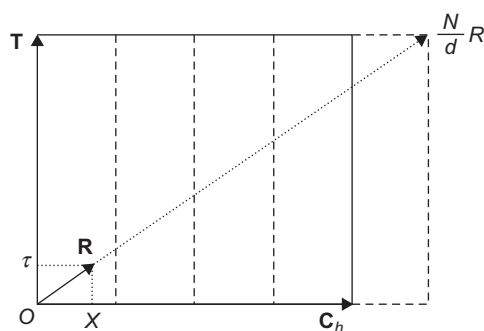
FIGURE 18.18

Relation between **R**, **C**$_h$, and **T**·

Reproduced from Dresselhaus et al.[3] with the permission of Elsevier.

The projection of **R** on the **C**$_h$ and **T** axes yields ψ and τ. **X** in the figure is ψ scaled by

$$\mathbf{C}_h/2\pi.$$

18.3.5 Band Structure of a Fullerene Nanotube

The electronic band structure of a (10,10) fullerene nanotube was first calculated by Dresselhaus et al.[3] by using tight-binding methods and by using zone folding from the band structure of an infinite 2D graphene sheet. Their results are shown in Figure 18.19.

As one can see in Figure 18.19, the two bands that cross the Fermi energy at $ka = -2\pi/3$ have different symmetry and guarantee that the tube will be a metallic conductor.

FIGURE 18.19

Band structure of a (10,10) fullerene nanotube, calculated by Dresselhaus et al., using zone folding from the band structure of an infinite 2D graphene sheet.

Reproduced from Dresselhaus et al. (Ref. 3) with the permission of Elsevier.

18.4 POLYMERS

18.4.1 Introduction

A long chain of molecules that has a backbone of carbon atoms is known as a polymer. The basic building block, which usually but not necessarily consists of one carbon atom and two hydrogen atoms, is known as a monomer. A polymer is formed by repeating the structure of the monomer over and over again. In fact, a single polymer can be constituted from several thousand monomers.

Materials composed from polymers, such as bone, wood, skin, and fibers, have been used by man since prehistoric times. However, polymer science was developed in the twentieth century by Hermann Staudinger, who developed the concept of macromolecules in the 1920s. Wallace Carothers showed the great industrial potential of synthetic polymers and invented nylon in 1935. Synthetic polymers are now used in large quantities in a variety of applications. In the 1950s, Ziegler and Natta discovered polymerization catalysts, which led to the development of the modern plastics industry. Some of the most popularly known polymers are rubber, plastic, and Teflon. They do not have any common property other than the fact that they are lightweight, flexible, resistant to corrosion, and easy to

mold or cut into any desired shape. Some polymers such as rubber are very elastic and can be deformed very easily. Other polymers that have similar elastic property to rubber are known as elastomers.

Paul Flory created modern polymer science through both experimental and theoretical studies of "macromolecules." A polymer is essentially a giant molecule. There are a variety of ways in which giant molecules can be obtained. Other examples of such giant molecules are branched polymers, in which hydrogen atoms are replaced by any of the halogen elements that need one electron to have a filled subshell. When the hydrogen atoms are replaced by molecules, more complex polymers are obtained. A third alternative is that the carbon chain can be replaced by silicon atoms. In view of the fact that there is a huge variety of ways in which polymers can be obtained, and the fact that they can be easily and cheaply produced, there is a great deal of excitement in finding new ways of obtaining and using complex polymers.

18.4.2 **Saturated and Conjugated Polymers**

In the saturated polymers studied by Staudinger, Flory, Ziegler, and Natta, all four valence electrons of carbon are used up in covalent bonds, and hence, they are insulators. Therefore, they are viewed as unsuitable for use as electronic materials. In contrast, in conjugated polymers, the chemical bonding leads to one unpaired electron (the π electron) per carbon atom. The carbon orbitals are in the sp^2p_z configuration in the π bonding. Because the orbitals of the successive carbon atoms overlap, the electrons are delocalized along the backbone of the polymer, which provides the path for charge mobility along the polymer chain. The molecular structure of some conjugated polymers is shown in Figure 18.20. The bond-alternated structure of polyacetylene is characteristic of conjugated polymers, which are typically semiconductors.

The electronic structure of conducting polymers can be determined by the symmetry of the chain. These polymers can exhibit either metallic or semiconducting properties. These electrically conducting polymers are known as the "fourth generation of polymeric materials."

The electronic structure in conducting polymers is determined by the number and kinds of atoms within the repeat unit (chain symmetry). The classic example is *trans-* and *cis-*polyacetylene, $(-CH)_n$, which is shown in Figure 18.21.

In polyacetylene, if the carbon–carbon bond lengths were equal, the chemical formula, $(-CH)_n$ with one unpaired electron per formula unit, would yield a metallic state. If the electron–electron interactions were too strong, $(-CH)_n$ would be an antiferromagnetic Mott insulator, a possibility that has been eliminated through a variety of studies together with the fact that these are easily converted to a metallic state on doping.

The structure in polyacetylene is dimerized due to Peierls instability with two carbon atoms in the repeat unit, $(-CH = CH)_n$. Thus, the π band is divided into π and π^* bands, each of which can hold two electrons per atom (spin-up and spin-down). The $\pi - \pi^*$ energy gap E_g implies that there are no partially filled bands and polyacetylene is a semiconductor. However, the electrical conductivity of polyacetylene can be increased by more than a factor of 10^7 to a level approaching that of a metal by using a dopant. The electrical conductivity of *trans-*(CH), as a function of (AsF_5) dopant concentration, is shown in Figure 18.22.

However, until 1990, there were no known examples of stable metallic polymers. It was shown that polyaniline (PANI) could be rendered, conducting either through oxidation of the
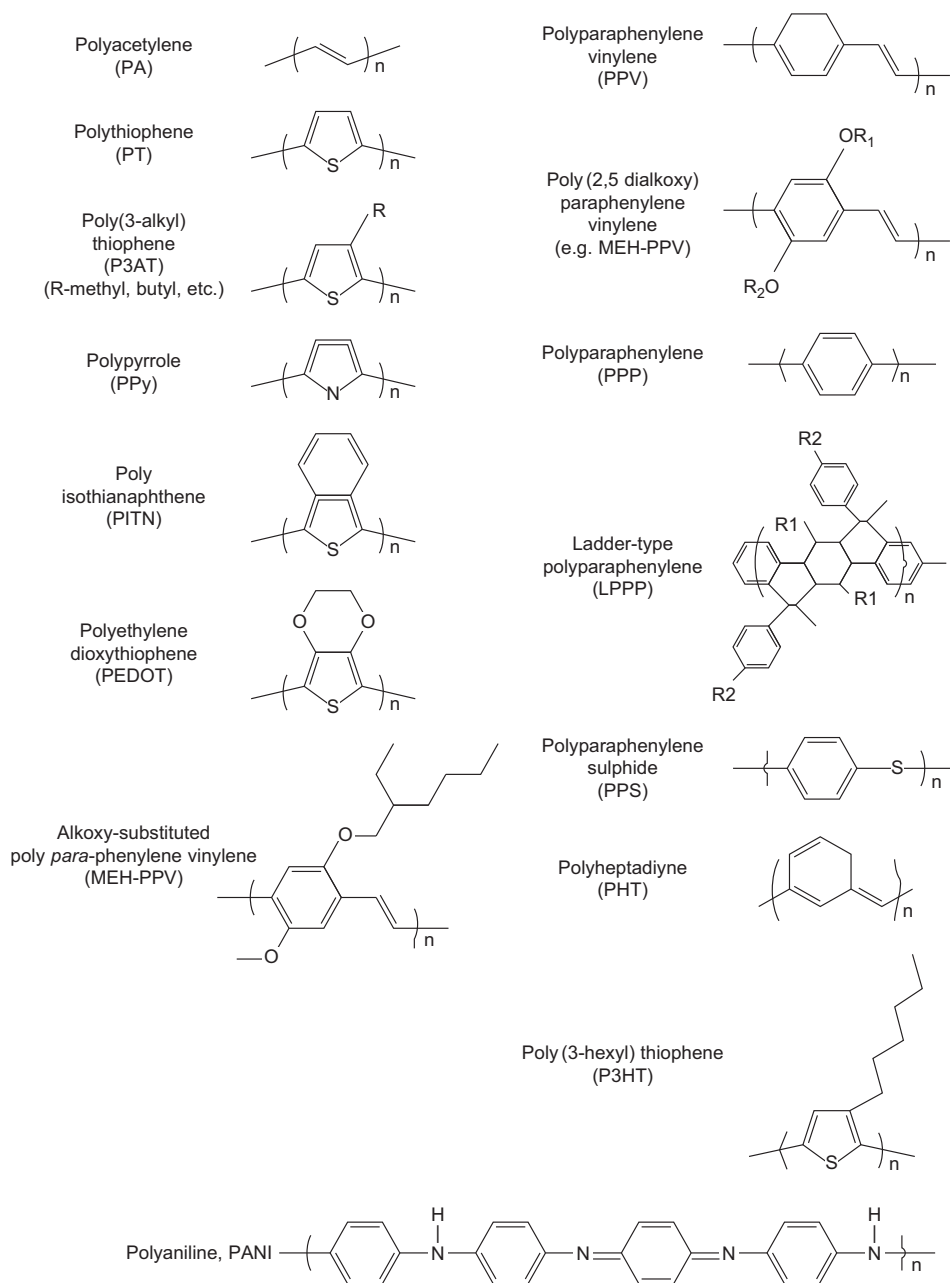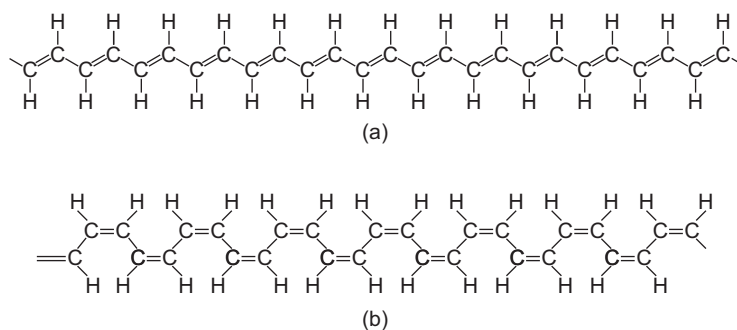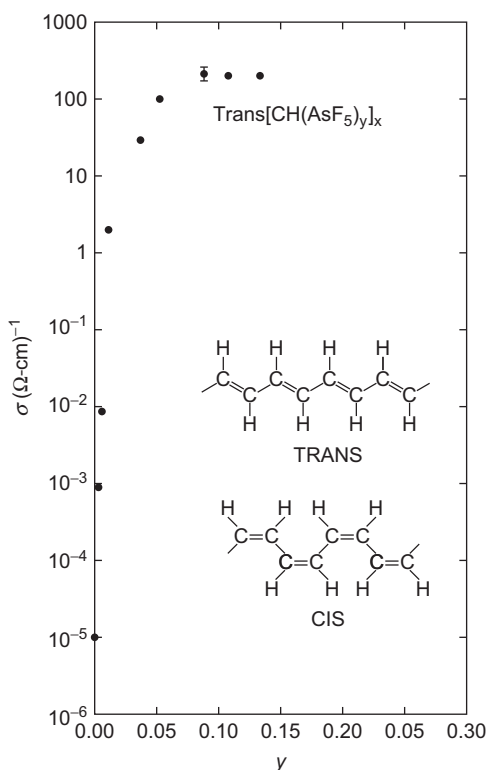
FIGURE 18.20

Molecular structures of some conjugated polymers (bond-alternated structures).

Reproduced from Heeger[6] with the permission of the American Physical Society.

FIGURE 18.21

(a) All *trans*- and (b) all *cis*-polyacetylene.

FIGURE 18.22

Electrical conductivity of *trans*-(CH) as a function of (AsF$_5$) dopant concentration.

Reproduced from Heeger[6] with the permission of the American Physical Society.

leucoemeraldine base or protonation of the emeraldine base. Eventually, protonic acids were used to both convert PANI to metallic form and render the resulting PANI complex soluble in common organic solvents. The processibility of PANI induced by the "surfactant" counterions has made possible the fabrication of conducting polymer blends with a variety of host polymers. The "surfactant" counterions led to the formation of a self-assembled network, due to which the PANI network remains connected and conducting even after the removal of the host polymer. This led to the fabrication of novel electrodes for use in electronic devices.

The chemistry and physics of these polymers in the semiconducting state are also of great interest since their application to "plastic electronic" devices. The polymer diodes were fabricated in the 1980s and the light-emitting diodes (LEDs) in 1990. The other "plastic" optoelectronic devices include lasers, high-sensitivity plastic photodiodes, photovoltaic cells, ultrafast image processors, thin-film transistors, and all-polymer integrated circuits. All these are fabricated semiconducting and metallic polymers that are thin-film devices in which the active layers are fabricated by casting the semiconducting and/or metallic polymers from solution.

18.4.3 **Transparent Metallic Polymers**

In conventional metals, the length of the interchain spacing and of the repeat unit are large compared to the interatomic distances. However, in metallic polymers, N, the number of electrons per unit volume is on the order of $N \sim 2 - 5 \times 10^{21}$ cm^{-3}. The plasma frequency (the frequency below which the metals reflect light) is given by

$$\omega_p^2 = 4\pi Ne^2/m^*, \tag{18.52}$$

where m^* is the effective mass of the electrons. Thus, the plasma frequency of metallic polymers is on the order of 1 eV. Hence, they are semitransparent in the visible part of the spectrum but exhibit high reflectance in the infrared. Therefore, optical-quality thin films of metallic polymers are used as transparent electrodes. Transparent conducting films are used as antistatic coatings, as electrodes in liquid-crystal display cells or in polymer LEDs, or for fabricating electrochromic windows.

18.4.4 **Electronic Polymers**

Electronic polymers are those polymers of which the conductivity can be increased by several orders of magnitude, which can be obtained by doping. The increase of conductivity of electronic polymers by doping is shown in Figure 18.23.

In Figure 18.23, *trans*-(CH)$_x$ and the emeraldine base form of polyamine are shown to give an example of the increase in electrical conductivity by doping. Electronic polymers are extensively used in light-emitting diodes. In addition, superconductivity has been discovered in regioregular
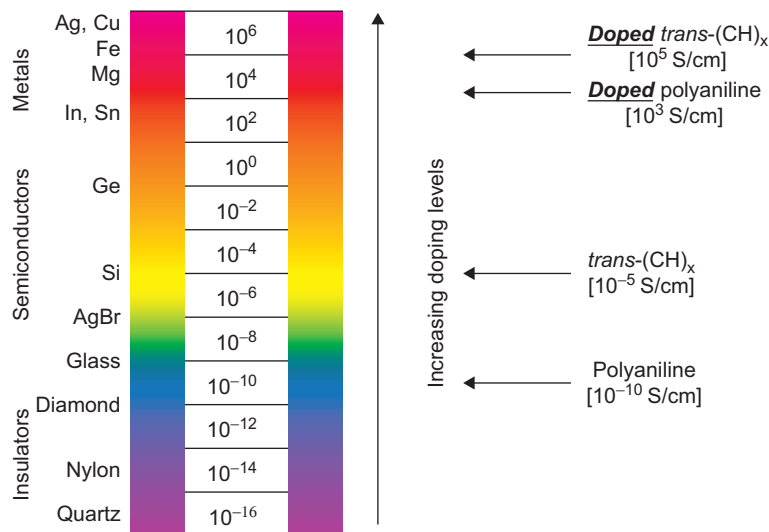

FIGURE 18.23

Increase of conductivity of electronic polymers by doping.

Reproduced from MacDiarmid[11] *with the permission of the American Physical Society.*

poly (3-hexylthiophene) around a critical temperature of 2° K. The future application of this amazing discovery is still being speculated.

18.5 SOLITONS IN CONDUCTING POLYMERS

18.5.1 Introduction

Trans-polyacetylene (*trans*-$(CH)_x$) was the first highly conducting organic polymer. The simple molecular structure $-CH-$ units are repeated, which implies that each carbon contributes a single p_z electron to the π band, and as a result, the π band would be half-filled. Thus, polyacetylene would be a one-dimensional metal. However, in 1955, Peierls showed that 1D metals are unstable with respect to a structural distortion that opens up an energy gap at the Fermi level; thereby, 1D metals end up as semiconductors. The periodicity of the Peierls distortion is $\Lambda = \pi/k_F$, where the Fermi wave vector $k_F = 2\pi/a$ for the half-filled band of *trans*-$(CH)_x$. Hence, it converts *trans*-polyacetylene into *trans*-$(-HC = CH-)_x$, which is essentially alternating single and double bonds, as shown in Figure 18.24a.

However, a chain of monomers can be dimerized in two distinct patterns, both of which have the same energy (the degenerate *A* and *B* phases), as shown in Figure 18.24b.

Thus, in addition to electron and hole excitations in a dimerized semiconductor, a domain wall separates regions of different bonding structures or different vacua, which would be a new type of excitation. The large width of the domain walls leads to a small effective mass for the excitations, on the order of electron mass instead of the ionic mass. The domain-wall excitation, which propagates freely, has been called a "soliton." Because a moving soliton converts $A-$ phase material into $B-$ phase material (or vice versa), these objects can only be created or destroyed in pairs. The creation of a soliton is shown in Figure 18.24c.

As we will see, because the midgap state is a solution to the Schrodinger equation in the presence of the structural kink, it can be occupied with zero, one, or two electrons. However, a charged soliton, which has either zero or two electrons in the gap state, carries a charge $\pm e$ and has spin zero, rather than the spin $\frac{1}{2}$ as for an electron or a hole. These reversed spin-charge relations are a fundamental feature of the soliton model of polyacetylene and are supported by experiment.

The π band of $(CH)_x$ is split into two subbands: a fully occupied π band (valence band) and an empty π^* band (the conduction band), each with a wide bandwidth (~ 5 eV) and significant distortion. The resulting band structure results from the opening of the band gap that originates from the doubling of the unit cell. This is shown in Figure 18.25.
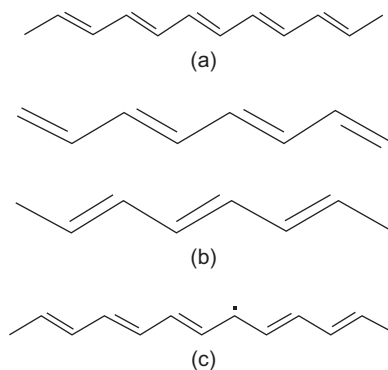
(a)

(b)

(c)

FIGURE 18.24

(a) Dimerized structure due to Peierls instability. (b) Degenerate *A* and *B* phases of dimerized structure. (c) Soliton in *trans*-polyacetylene.
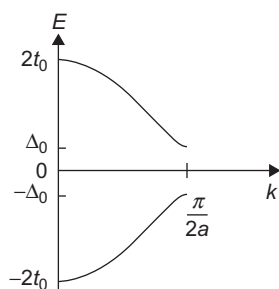
FIGURE 18.25

Band structure of polyacetylene. Energy opening at $k = 2\pi/a$ due to Peierls distortion.

18.5.2 **Electronic Structure**

The electronic structure of conjugated polymers (SSH) was described by Su et al.[17] by using a tight-binding model in which the π electrons are coupled to distortions in the polymer backbone by the electron–phonon interaction. In the SSH model, photoexcitation across the $\pi - \pi^*$ band gap creates the excitations of conducting polymers: solitons (in degenerate ground-state systems), polarons, and bipolarons. Direct photogeneration occurs due to the overlap between the uniform chain in the ground state and the distorted chain in the excited state.

18.5.3 **Tight-Binding Model**

Each (CH) group (Figure 18.26) has six degrees of freedom for nuclear translation. Su et al.[17] postulated that only the dimerization coordinate u_n, which specifies the displacement of the nth group along the molecular symmetry group, is important. The tight-binding Hamiltonian can be written as

$$
\begin{aligned}
H &= H_\pi + H_{\pi-ph} + H_{ph} \\
&= \sum_{n,s}[-t_0 + \alpha(u_{n+1} - u_n)](c^{\dagger}_{n+1,s}c_{n\cdot s} + c^{\dagger}_{n,s}c_{n+1,s}) + \sum_n\left[\frac{p_n^2}{2M} + \frac{1}{2}K(u_{n+1} - u_n)^2\right],
\end{aligned}
\tag{18.53}
$$

where p_n are the nuclear momenta, u_n are the displacements from equilibrium, M is the carbon mass, and K is an effective spring constant. The $c^{\dagger}_{n,s}$, $c_{n,s}$ are the fermion creation and annihilation operators for site n. The first term describes the hopping of $\pi(p_z)$ electrons along the chain without spin flip. The second term describes the $\pi-$ electron–phonon interaction where the terms linear in u_n dominate higher-order terms for the weak-coupling systems. The last two terms are, respectively, a harmonic "spring constant" term, which represents the increase in potential energy that results from displacement from the uniform bond lengths in $(CH)_x$, and a kinetic energy term, where M is the mass of the (CH) group and p_n is the momentum conjugate to u_n.
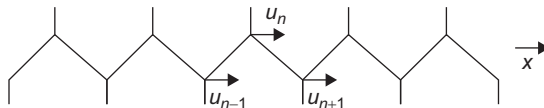

FIGURE 18.26

Dimerization coordinate u_n defined for *trans*-$(CH)_x$.

18.5.4 **Soliton Excitations**

The ground state of a one-dimensional metal is spontaneously distorted to form a charge-density wave $<u_n> \neq 0$, as per Peierls theorem. The strongest instability occurs for a charge-density wave of wave number $Q = k_F = \pi/a$, and hence, we consider the adiabatic ground-state energy E_0 as a function of the mean amplitude of distortion u, where the u_n's are considered to be

$$u_n \rightarrow <u_n> = (-1)^n u. \tag{18.54}$$

For u_n given by Eq. (18.54), $H_{\pi-ph}$ is invariant under spatial translation $2ma$, $m = \pm1, \pm2, ...$, and H can be diagonalized in k space in the reduced zone, $-\pi/2a < k < \pi/2a$, for the valence $(-)$ and conduction $(+)$ bands. For a chain of monomers of ring geometry, we obtain (Problem 18.6)

$$\hat{H}(u) = -\sum_{n,s}[t_0 + (-1)^n 2\alpha u](\hat{c}_{n+1,s}^\dagger \hat{c}_{n,s} + \hat{c}_{n,s}^\dagger \hat{c}_{n+1,s}) + 2NKu^2. \tag{18.55}$$

For $\alpha = 0$, $H(u)$ can be made diagonal by using the Bloch operators,

$$\hat{c}_{ks} = (N^{-1/2}) \sum_{n,s} e^{-ikna} \hat{c}_{ns} \tag{18.56}$$

in the extended zone, where $-\pi/a < k \leq \pi/a$.

For $\alpha \neq 0$, the big zone can be folded into the little zone, as shown in Figure 18.27. The valence- and conduction-band operators are defined as

$$\hat{c}_{ks-} = (N)^{-1/2} \sum_{n,s} e^{-ikna} \hat{c}_{ns} \tag{18.57}$$

and

$$\hat{c}_{ks+} = -i(N)^{-1/2} \sum_{n,s} e^{-ikna} (-1)^n \hat{c}_{ns}. \tag{18.58}$$

From Eqs. (18.55), (18.57), and (18.58), we obtain (Problem 18.8)

$$\hat{H}(u) = \sum_{ks} \left[\varepsilon_k (\hat{c}_{ks+}^\dagger \hat{c}_{ks-} - \hat{c}_{ks-}^\dagger \hat{c}_{ks-}) + \Delta_k (\hat{c}_{ks+}^\dagger \hat{c}_{ks-} + \hat{c}_{ks-}^\dagger \hat{c}_{ks+}) \right] + 2NKu^2, \tag{18.59}$$

FIGURE 18.27

The reduced and extended zone schemes.

where Δ_k, the energy gap parameter, is defined as
$$\Delta_k = 4\alpha u \sin ka. \tag{18.60}$$

In the reduced zone, the unperturbed band energy is defined as

$$\varepsilon_k = 2t_0 \cos ka, \quad (-\pi)/(2a) < k < (\pi)/(2a), \tag{18.61}$$

where ε_k describes particles for $(+)$ and holes for $(-)$. We now convert H in Eq. (18.59) to a diagonal form by making the transformation

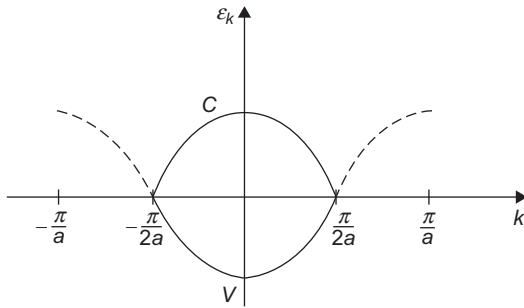$$\hat{a}_{ks-} = \alpha_k \hat{c}_{ks-} - \beta_k \hat{c}_{ks+}$$

and

$$\hat{a}_{ks+} = \beta_k \hat{c}_{ks-} + \alpha_k \hat{c}_{ks+}. \tag{18.62}$$

We have, in analogy with BCS theory of superconductivity,

$$|\alpha_k|^2 + |\beta_k|^2 = 1, \tag{18.63}$$

so that the a's satisfy the Fermi anticommutation relations. Because H has no term that mixes the $(+)$ and $(-)$ operators, we obtain from Eq. (18.59) through (18.62)

$$H = \sum_k E_k(n_{ks+} - n_{ks-}) + 2NKu^2. \tag{18.64}$$

The quasiparticle energy is given by (in analogy with BCS superconductivity theory)

$$E_k = (\epsilon_k^2 + \Delta_k)^{1/2}, \tag{18.65}$$

$$\alpha_k = [(1 + \varepsilon_k/E_k)/2)]^{1/2}, \tag{18.66}$$

$$\beta_k = [(1 - \varepsilon_k/E_k)/2)]^{1/2} \ \text{sgn} \ \Delta_k, \tag{18.67}$$

and

$$\alpha_k \beta_k = \Delta_k/(2E_k). \tag{18.68}$$

If one were to clamp u_n at the ground-state mean-field value, $(-1)^n u$, the chain would behave as a conventional semiconductor with electron and hole excitations. However, because of the two-fold-degenerate ground-state $E(u_0) = E(-u_0)$, the system supports nonlinear excitations, which act as moving walls separating the A phase $(+u_0)$ and B phase $(-u_0)$. This is shown in Figure 18.28, which implies that the nonlinear excitations, solitons, will bef important. To determine the soliton, one introduces

$$\varphi_n = (-1)^n u_n, \tag{18.69}$$

so that in the A phase, $\varphi_n = u_0$, and in the B phase, $\varphi_n = -u_0$. However, numerical calculations have shown that the form of φ_n, for the preferred width ξ of the soliton that minimizes the total energy, is

$$\varphi_n = u_0 \tanh[(n - n_0)a/\xi)]. \tag{18.70}$$

It has been calculated that $\xi \approx 7a$, and the energy to create a soliton at rest is $E_s \approx 0.42$ eV. Thus, $E_s < 0.5 \ \Delta$, where Δ is the single-particle gap. Thus, it is less costly to create a soliton than an electron or hole, and they are spontaneously generated by photoexcitation, by thermal generation, or by injection of electrons and/or holes. It
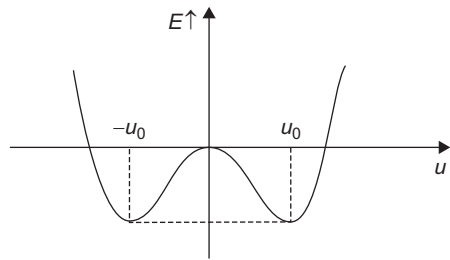

FIGURE 18.28

The total energy of the dimerized polyacetylene chain.

can also be shown that for each widely spaced soliton or antisoliton (a reverse boundary from the *B* phase back to the *A* phase), there exists a normalized single-electron state in the gap center that can accommodate zero, one, or two electrons.

18.5.5 Solitons, Polarons, and Polaron Excitations

It can be seen from Figure 18.29c that because the nonbonding or atomic state formed by the chain relaxation can be mapped to a specific atomic site, the resulting distribution of charge and spin can be understood. If the state is unoccupied (doubly occupied), the carbon atom at the boundary is left with a positive (negative) charge, but there are no unpaired spins. Therefore, the charged soliton is positively (negatively) charged but spinless. Single occupation of the soliton state neutralizes the electronic charge of the carbon nucleus, while introducing an unpaired spin onto the chain. The localized electronic state associated with the soliton is a nonbonding state at an energy that lies at the middle of the $\pi - \pi^*$ gap, between the bonding and antibonding levels of the perfect chain.
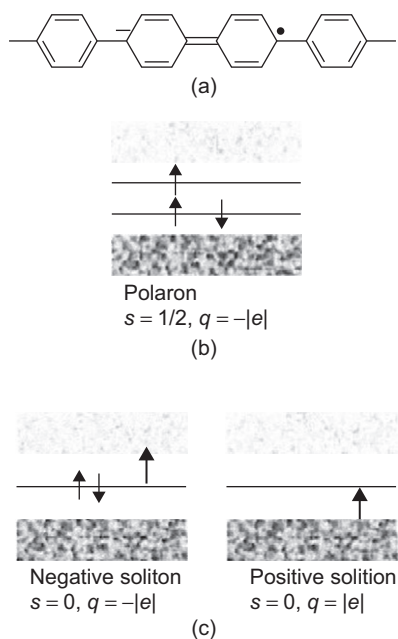

(a)

Polaron
$s = 1/2, q = -|e|$
(b)

Negative soliton   Positive solition
$s = 0, q = -|e|$ $s = 0, q = |e|$
(c)

FIGURE 18.29

(a) Schematic picture of a polaron in polyparaphenylene (PPP); (b) band diagram of an electron polaron—the lower gap state is single occupied and the upper gap state is empty for a hole polaron; (c) band diagrams for positive and negative solitons.

Reproduced from Heeger[6] with the permission of the American Physical Society.

18.6.6 Polarons and Bipolarons

A polaron can be thought of as a bound state of a charged soliton and a neutral soliton of which the midgap energy states hybridize to form bonding and antibonding levels. The neutral soliton contributes no charge and a single spin. The charged soliton carries a charge of $\pm e$ and no spin. The resulting polaron is a fermion with the charge-spin relationship $q = \pm e$ and $s = 1/2$. The positive polaron is a radical cation; the negative polaron is a negative anion. Both are quasiparticles consisting of a single electronic charge dressed with a local geometrical relaxation of the bond lengths. The schematic picture of polarons in PPP is shown in Figures 18.29a and b.

A bipolaron is a bound state of two charged solitons of like charges or two polarons of which the neutral solitons annihilate each other with two corresponding midgap levels. The bipolarons are shown in Figure 18.30. Because each charged soliton has a single electronic charge and no spin, the bipolaron has charge $\pm 2e$ and zero spin. Both positive and negative bipolarons are doubly charged bound states of two polarons bound together by enhanced geometrical relaxation of the bond lengths or the overlap of a common lattice distortion.
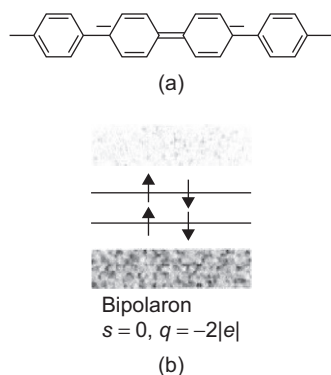
(a)

Bipolaron
$s = 0, q = -2|e|$

(b)

FIGURE 18.30

Bipolarons in polymer with nondegenerate ground
state. (a) Negative bipolaron in PPP; (b) band
diagram for a negative bipolaron. For a positive
bipolaron, both gap states are unoccupied.

*Reproduced from Heeger[6] with the permission of the American
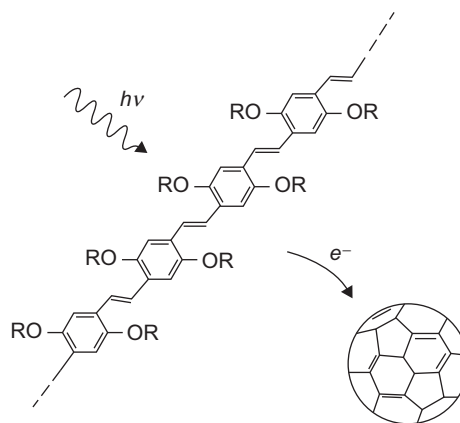Physical Society.*

FIGURE 18.31

Photoinduced electron transfer from a conjugated
semiconducting polymer to C_{60}.

*Reproduced from Heeger[6] with the permission of the American
Physical Society.*

18.6 PHOTOINDUCED ELECTRON TRANSFER

The electrons are promoted to the antibonding π^* band of semiconducting polymers when they are photo-
excited. The photoinduced nonlinear excitations (such as polarons) on the conjugated polymer backbone
are quite stable. Thus, semiconducting polymers are electron donors when they are photoexcited. On the
other hand, Buckministerfullerene, C_{60}, is an excellent electron acceptor capable of accepting up to six
electrons. It forms charge-transfer salts with several types of donors. The photoinduced transfer process
from a conjugated semiconducting polymer to C_{60} is shown schematically in Figure 18.31.

A study of the dynamics of the photoinduced electron transfer from semiconducting polymers to C_{60}
by Lanzani et al. (Ref. 10) demonstrated that the charge transfer occurs within 50 fs after photoexcita-
tion. This charge transfer rate is more than 1000 times faster than any other process. The quantum
efficiency for charge separation approaches one. In addition, the charge separation state is metastable.

PROBLEMS

18.1. Show that the reciprocal lattice vectors of honeycomb lattice of graphene (Figure 18.3) are

$$\mathbf{b}_1 = \frac{2\pi}{3a}(\hat{i} + \sqrt{3}\hat{j}); \ \ \mathbf{b}_2 = \frac{2\pi}{3a}(\hat{i} - \sqrt{3}\hat{j}). \tag{1}$$

18.2. Show that the positions of the two Dirac points K and K', located at the corners of the
Brillouin zone (Figure 18.3), are

$$\mathbf{K} = \frac{2\pi}{3a}\left(\hat{i} + \frac{1}{\sqrt{3}}\hat{j}\right); \ \ \mathbf{K}' = \frac{2\pi}{3a}\left(\hat{i} - \frac{1}{\sqrt{3}}\hat{j}\right). \tag{1}$$

18.3. Show that by substituting in Eq. (18.6),

$$H\psi = E\psi, \tag{1}$$

we obtain

$$H_{11} + \lambda H_{12} = E \tag{2}$$

and

$$H_{12} + \lambda H_{22} = \lambda E. \tag{3}$$

Here,

$$H_{11} = \int \phi_1{}^* H\phi_1 \, d\nu, \ H_{12} = H_{21}{}^* = \int \phi_1{}^* H\phi_1 \, d\nu; \ H_{22} = \int \phi_2{}^* H\phi_2 \, d\nu \tag{4}$$

and

$$\int \phi_1{}^* \phi_1 d\nu = \int \phi_2{}^* \phi_2 d\nu = 1. \tag{5}$$

18.4. It has been shown in Eq. (18.19) that

$$H_{11} = \frac{1}{N} \sum_{A,A'} e^{-i\mathbf{k}\cdot(\mathbf{r}_A - \mathbf{r}_{A'})} \int \chi^* (\mathbf{r} - \mathbf{r}_A) H\chi(\mathbf{r} - \mathbf{r}_{A'}) \, d\nu. \tag{1}$$

Keeping only the nearest-neighbor integrals among the atoms A, and writing

$$E_0 = \int \chi^* (\mathbf{r}) H\chi(\mathbf{r}) \, d\nu \tag{2}$$

and

$$\gamma_0' = -\int \chi^* (\mathbf{r} - \overrightarrow{\rho}') H\chi(\mathbf{r}) \, d\nu, \tag{3}$$

where $\overrightarrow{\rho}' = \mathbf{a}_1 (say)$ is a vector joining the nearest neighbor among atoms A, show that

$$H_{11} = E_0 - 2\gamma_0'[\cos(2\pi k_y a) + 2\cos(\pi k_x a\sqrt{3})\cos(\pi k_y a)]. \tag{4}$$

18.5. It has been shown in Eq. (18.28) that

$$H_{12} = \frac{1}{N} \sum_{A,B} e^{-i\mathbf{k}\cdot(\mathbf{r}_A - \mathbf{r}_B)} \int \chi^* (\mathbf{r} - \mathbf{r}_A) H\chi(\mathbf{r} - \mathbf{r}_B). \tag{1}$$

Considering only the nearest-neighbor interactions in the lattice (between atoms of type A and type B and vice versa), we write (in analogy with Eq. 18.27)

$$\gamma_0 = \int \chi^*(\mathbf{r} - \overrightarrow{\rho})(U - V)\chi(\mathbf{r}) \, dv > 0, \tag{2}$$

where

$$\overrightarrow{\rho} = \mathbf{AB}. \tag{3}$$

Show that

$$H_{12} = -\gamma_0[e^{-ik_xa} + 2\cos(\sqrt{3}k_ya)e^{3ik_xa/2}] \tag{4}$$

and

$$|H_{12}|^2 = \gamma_0^2\left[1 + 4\,\cos^2\left(\frac{\sqrt{3}}{2}k_ya\right) + 4\,\cos\left(\frac{\sqrt{3}}{2}k_ya\right)\,\cos\left(\frac{3}{2}k_xa\right)\right]. \tag{5}$$

18.6. The translation vector of a general chiral tubule can be written as

$$\mathbf{T} = [(2m+n)\mathbf{a}_1 - (2n+m)\mathbf{a}_2]/d_R. \tag{1}$$

The length T of the translation vector $\mathbf{T}$ corresponds to the first lattice point of the graphene sheet. Show that

$$T = \sqrt{3}C_h/d_R, \tag{2}$$

where the length C_h is defined in Eq. (18.47). Defining d as the highest common divisor of (n, m), we have

$$d_R = \begin{cases} d & \text{if } n-m \text{ is not a multiple of } 3d \\ 3d & \text{if } n-m \text{ is a multiple of } 3d. \end{cases} \tag{3}$$

18.7. The tight-binding Hamiltonian for the polymer *trans*-(CH)$_x$ is given by (Eq. 18.53)

$$\begin{aligned} H &= H_\pi + H_{\pi-ph} + H_{ph} \\ &= \sum_{n,s}[-t_0 + \alpha(u_{n+1} - u_n)](\hat{c}_{n+1,s}^\dagger\hat{c}_{n.s} + \hat{c}_{n,s}^\dagger\hat{c}_{n+1,s}) + \sum_n\left[\frac{p_n^2}{2M} + \frac{1}{2}K(u_{n+1} - u_n)^2\right]. \end{aligned} \tag{1}$$

Show that if

$$u_n \rightarrow <u_n> = (-1)^nu, \tag{2}$$

one can write

$$H(u) = -\sum_{n,s}[t_0 + (-1)^n2\alpha u](\hat{c}_{n+1,s}^\dagger\hat{c}_{n,s} + \hat{c}_{n,s}^\dagger\hat{c}_{n+1,s}) + 2NKu^2 \tag{3}$$

for a chain of monomers in a ring geometry.

18.8. Show that for $\alpha = 0$, $H(u)$ in Eq. (3) of Problem 18.7 can be made diagonal by using the Bloch operators,

$$\hat{c}_{ks} = (N^{-1/2})\sum_{n,s}e^{-ikna}\hat{c}_{ns}, \tag{1}$$

in the extended zone, where $-\pi/a < k \leq \pi/a$.

18.9. Show that by using the operators

$$\hat{c}_{ks-} = (N)^{-1/2}\sum_{n,s} e^{-ikna}\,\hat{c}_{ns} \tag{1}$$

and

$$\hat{c}_{ks+} = -i(N)^{-1/2}\sum_{n,s} e^{-ikna}(-1)^n\hat{c}_{ns}, \tag{2}$$

Eq. (3) in Problem 18.7 can be rewritten as

$$H(u) = \sum_{ks}\left[\varepsilon_k(\hat{c}_{ks+}^{\dagger}\hat{c}_{ks-} - \hat{c}_{ks-}^{\dagger}\hat{c}_{ks-}) + \Delta_k(\hat{c}_{ks+}^{\dagger}\hat{c}_{ks-} + \hat{c}_{ks-}^{\dagger}\hat{c}_{ks+})\right] + 2NKu^2, \tag{3}$$

where Δ_k, the energy gap parameter, is defined as

$$\Delta_k = 4\alpha u \sin ka. \tag{4}$$

18.10. From Eqs. (18.59) through (18.62), show that

$$H = \sum_k E_k(n_{ks+} - n_{ks-}) + 2NKu^2. \tag{1}$$

References

1. Castro Neto AH, Guinea F, Peres NMR, Noboselov KS, Geim AK. The electronic properties of graphene. *Rev Mod Phys* 2009;**81**:109.
2. Curl RF. Dawn of the fullerenes: experiment and conjecture. *Rev Mod Phys* 1997;**69**:691.
3. Dresselhaus MS, Dresselhaus G, Ekland PC. *Science of fullerenes and nanoparticles*. Amsterdam: Elsevier Science; 1996.
4. Dresselhaus MS, Dresselhaus G, Saito R. Physics of Carbon Nanotubes. *Carbon* 1995;**33**:883.
5. Geim AK, Novoselov KS. The rise of Graphene. *Nature materials* 2007;**6**:183.
6. Heeger AJ. Semiconducting and metallic polymers: The fourth generation of polymeric materials. *Rev Mod Phys* 2001;**73**:681.
7. Heeger AJ, Kivelson S, Schrieffer JR, Su W-P. Solitons in conducting Polymers. *Rev Mod Phys* 1988;**60**:781.
8. Kroto HW. Symmetry, space, stars and C60. *Rev Mod Phys* 1997;**69**:703.
9. Kroto HW, Heath JR, O'Brien SC, Curl RF, Smalley RE. C60: Buckminsterfullerene. *Nature* 1985; **318**:162.
10. Lanzani G, Zenz C, Cerullo G, Graupner W, Leising G, Scherf U, De Silvestri S. *Synth Met* 2000; **111–112**:493.
11. MacDiarmid AG. "Synthetic Metals." A novel role for organic polymers. *Rev Mod Phys* 2001;**73**:701.
12. Malard LM, Pimenta MA, Dresselhaus G, Dresselhaus MS. Raman Spectroscopy in Graphene. *Phys Rep* 2009;**473**:51.
13. Novoselov KS, Geim AK, Morozov SV, Jiang D, Zhang Y, Grigoneva IV, et al. Electric field effect in atomically thin carbon films. *Science* 2004;**306**:666.

14. Novoselov KS, Geim AK, Morozov SV, Jiang D, Katsnelson MI, Grigoneva IV, et al. Two-dimensional gas of massless Dirac fermions in graphene. *Nature* 2005;**438**:197.
15. Novoselov KS, Jiang D, Schedin F, Booth TJ, Khotkevich VV, Morozov SV, et al. Two-dimensional atomic crystals. *Proc Natl Acad Sci* 2005;**102**:10451.
16. Smalley RE. Discovering the fullerenes. *Rev Mod Phys* 1997;**69**:723.
17. Su WP, Schrieffer JR, Heeger AJ. Solitons in Polyacetylene. *Phys Rev Lett* 1979;**42**:1698.
18. Taylor R, Hare JP, Abdul-Sada AK, Kroto J. *Chem Soc Chemical Commu* 1990;1423.
19. Wallace PR. The Band Theory of Graphite. *Phys Rev* 1947;**71**:622.